Mid-infrared photoluminescence and internal quantum efficiency of InAs core/shell nanowires with InGaAs, AlSb and GaSb shells

Xiren Chen,[†] H. Alradhi,[‡] Zh. M. Jin,[‡] Liangqing Zhu,[†,¶] A. M. Sanchez,[§] Qiandong Zhuang,[*,‡] and Jun Shao[*,†]

†State Key Laboratory of Infrared Physics, Shanghai Institute of Technical Physics, Chinese Academy of Sciences, 200083 Shanghai, China

‡Physics Department, Lancaster University, LA14YB Lancaster, United Kingdom

¶Engineering Research Center for Nanophotonics & Advanced Instrument, Ministry of Education, East China Normal University, 200062 Shanghai, China

§Physics Department, Warwick University, CV47AL Coventry, United Kingdom

E-mail: q.zhuang@lancaster.ac.uk; jshao@mail.sitp.ac.cn

Abstract

Internal quantum efficiency (IQE) is an important figure of merit of semiconductors for photoelectric applications, whereas photoluminescence (PL) as a direct and powerful approach for clarifying carriers radiative recombination may serve as an efficacious tool to determine the IQE. While InAs core/shell (c/s) nanowires (NWs) are considered as the promising solution to reduce the optoelectronic limitation of surface states and for efficient quantum emission, the relationship between the IQE and shell coating remains unclear. In this work, pumping power- and temperature-dependent mid-infrared PL measurements are performed on a series samples of InAs c/s NWs with different shells

1

of InGaAs, AlSb and GaSb, together with a bare InAs NWs sample as core reference. Background carrier concentration is verified to be negligible in the PL process at 9 K, from which the IQE is successfully derived. Further analyses reveal that at 9 K the Auger recombination dominates and the IQE drops with the shell coating due mainly to the synergy of crystal quality deterioration in shell and particular radial band alignment, while the IQE gets significantly improved by up to about 50% for InGaAs shell coating at $40-140$ K, and up to about 20% beyond 110 K for AlSb shell coating, but no enhancement below 260 K for GaSb shell coating because mainly of the carriers leakage in type-III band alignment. The results indicate the potentiality of the c/s NWs for high-temperature IQE improvement and the availability of the PL analyses for clarifying the shell coating effects on the optoelectronic properties.

Keywords

InAs core/shell nanowires, internal quantum efficiency, mid-infrared photoluminescence, radiative recombination, pumping power- and temperature-dependence

Introduction

InAs nanowires (NWs) are promising for high-performance nanoscale infrared photoelectric applications of, e.g., laser diode,[1] solar cell,[2] and photodetector.[3] Considered as the potential solution for the key difficulty that the high-density surface dislocations hinder the the optoelectronic properties of InAs NWs, InAs core/shell (c/s) NWs have recently attracted intensive research interests, of which the radiative recombination behavior is widely concerned yet to be further clarified.[4–7]

Photoluminescence (PL) spectroscopy has been demonstrated as an efficient routine for characterizing the radiative recombination properties of nano semiconductors, as its intensity reflects directly the amount of emitting photons.[8–11] Significant enhancement of PL emission

has been verified in InAs/InP(As) c/s NWs, in contrast to the InAs NWs without shell.[4,7,12] As the effective absorption rate of pumping light and the number of photo-generated carriers as well are usually influenced by the NW distribution and NW geometry of the NW arrays,[13–15] direct comparison of PL intensity is unfair between different NWs samples, unless the NW samples with very similar density and morphology. This limitation can be relaxed if the concept of internal quantum efficiency (IQE) is employed, which serves as an important figure of merit of semiconductors for photoelectric applications and is defined as the ratio of the photon emission rate to the total electron-hole pair recombination rate.[5,16,17] Therefore, IQE may provide a pathway for comparing the radiative recombination properties of the InAs c/s NWs coated with different shells.
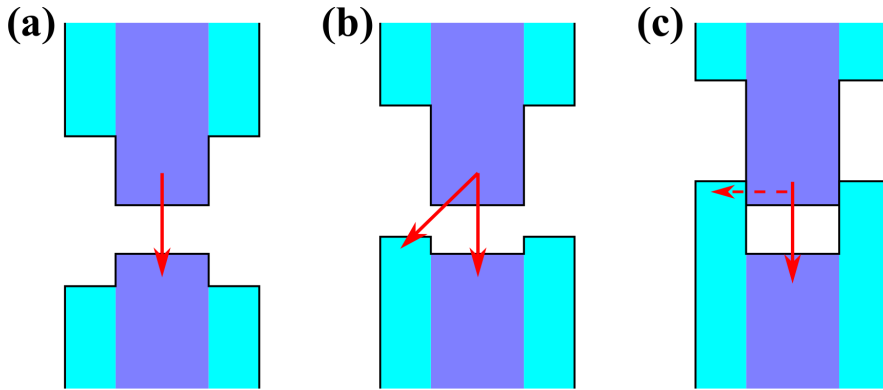

Figure 1: Schematic band structures of InAs c/s NWs with type-I (a), type-II (b) and type-III (c) band alignments. Solid-arrows for the radiative recombinations and dash-arrow for the transport of carriers in broken-gap structure.

As reported, InAs c/s NWs with different shells of, e.g., InP,[18] GaAs,[19] AlSb[6] and GaSb[20] had been synthesized. The c/s band alignment differs with the shell material, and hence determines carriers wave-function distributions and radiative recombination rate. The radial band alignments of InAs c/s NWs are typically classified into three types as schematically shown in Fig. 1.[21] In principle, the type-I band alignment allows merely the radiative recombination in the core of NW, while the type-II alignment may allow additional spatially-separated radiative transition between the electron in the core and the hole in the shell, because the conduction-band edge and valence-band edges (CBE and VBE) of the shell are

respectively higher than those of the core. A broken-gap structure, i.e., type-III band alignment,[21] will occur when the CBE of the core is below the VBE of the shell, in which radiative recombination is possible merely in the core, together with considerable leakage of the photogenerated carriers via radial transport.[22] In addition, lattice mismatch between the core and shell may bring strain, promote nonradiative rate due to crystal quality degradation and extra dislocations,[23] which will competes with the shell effect of surface passivation. As a result, the questions call for answers that how the radial band alignment and crystal quality affect the optoelectronic performance of, and what correlation between the IQE and different shells will be in the InAs c/s NWs?

We in this work select the InAs c/s NWs samples with InGaAs, AlSb and GaSb shells as the representatives of the type-I, type-II and type-III radial band alignments, respectively. The IQEs of these samples and a bare InAs NWs sample as core reference are derived with pumping power- and temperature-dependent PL experiments. Quantitative PL spectral analyses show that although the IQE declines with shell coating at very low temperature, a shell-induced enhancement shows up of up to 50% in the InAs/InGaAs c/s NWs in a temperature range of 40−140 K and of up to 20% in InAs/AlSb c/s NWs above 110 K. The results indicate potential advantages of the shell-coated InAs NWs for superiors high-temperature optoelectronic performance.

Experimental Details

The InAs/(InGaAs, AlSb, GaSb) c/s NWs samples were grown directly on n-type Si(111) substrates by molecular-beam epitaxy (MBE). Indium droplets acting as the nucleation site to prompt the InAs core growth was pre-calibrated prior to the NW growth. A substrate temperature range of around $420 − 460°C$ and an As_4 equivalent beam pressure of around $(6 − 9) \times 10^{-6}$ mbar were used for the InAs core growth. After the growth of the InAs core NWs, the deposition was followed of InGaAs, AlSb and GaSb shells, respectively. The

Ga content of the InGaAs shell is about $0.7 - 0.8$ as estimated by energy dispersive x-ray spectroscopy.

A step-scan Fourier-transform infrared (ssFTIR) spectrometer-based modulated PL technique was employed for the mid-infrared PL measurements.[24] A 532-nm continuous-wave laser was selected as the pumping source, its output was first accurately power-controlled by a laser power controller and then modulated by a mechanical chopper for optical pumping. A liquid-nitrogen cooled InSb detector was used for the PL signal detection and a lock-in amplifier for demodulation and amplification. The NWs samples were mounted on the cold finger of a closed-cycle compressor for temperature control. For the pumping power-dependent PL measurements, the samples' temperature was set at 9 K, while for temperature-dependent PL measurements the pumping power was set at 80 mW. More details about the modulated mid-infrared PL method and its advantages as well can be found elsewhere.[10,25–31]

Results and Discussions

Figure 2 depicts the scanning electron microscope (SEM) images together with corresponding single NW annular dark field (ADF) images of the InAs c/s NWs with InGaAs, AlSb and GaSb shells.

The c/s NWs are obviously bent, due to the non-uniform strain introduced by the shell.[32,33] The morphology distortion of the InAs/InGaAs c/s NWs as shown in Fig. 2(a) is most serious, because of the largest c/s lattice mismatch. Meanwhile, the large lattice mismatch leads to the misfit dislocations in shell as demonstrated by the ADF image around the InAs/InGaAs interface in Fig. 2(b). The InAs/AlSb c/s NWs manifest quite smooth surface morphology [Fig. 2(c)] whereas the InAs/GaSb c/s NWs exhibit rough NW surface morphology, as shown in the Fig. 2(d), which indicating the presence of significant disorder of crystal direction. The core diameters/shell thicknesses of the InAs/InGaAs, InAs/AlSb and InAs/GaSb c/s NWs are estimated as 46 nm/13 nm, 56 nm/5.6 nm and 121 nm/75
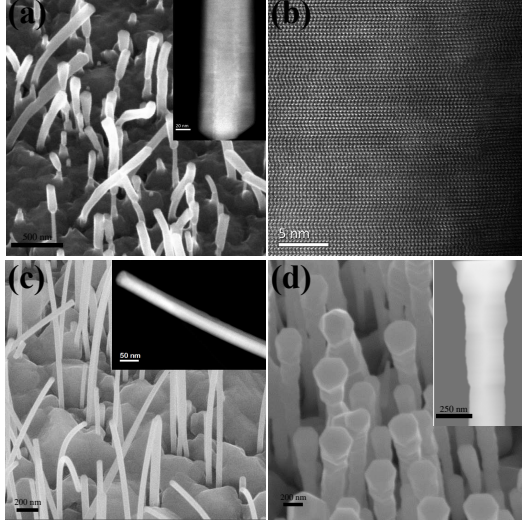
Figure 2: (a) Scanning electron microscope (SEM) and corresponding annular dark field (ADF, in the insert) images of the InAs/InGaAs c/s NWs. (b) ADF image around the InAs/InGaAs interface showing the significant misfit dislocations. (c) and (d) similar as (a), for the InAs/AlSb and InAs/GaSb c/s NWs, respectively.

nm, respectively. The InAs/InGaAs c/s NWs remain the type-I radial band alignment as the strain is insufficient for changing the band alignment,[21] while the InAs/GaSb c/s NWs maintain the type-III radial band alignment due to the insufficient core and/or shell quantum confinement.[34] For comparison, a bare InAs NWs sample with the zinc-blend/wurtzite (ZB/WZ) polytypic structure was used as the core reference.[10,35]

To inspect the radiative recombination properties, modulated PL measurements were carried out with the ssFTIR spectrometer-based technique,[24] by which the disturbance of environmental thermal emission was fully eliminated and weak mid-infrared PL signal was detectable.[10,36] Representative PL spectra are illustrated in Fig. 3 for different NWs samples at a temperature of 9 K under pumping powers of 10 mW and 320 mW, respectively.

The PL spectrum of the core reference sample under the low pumping can be decomposed into one dominant Gaussian-Lorentzian[37] feature that corresponding to the ZB conduction band-to-WZ valence band type-II transition, together with two weak features located at the low- and high-energy sides, which are ascribed to impurity-related and WZ bandgap transitions, respectively.[10,35] This assignment is supported by the fact that at high pumping power
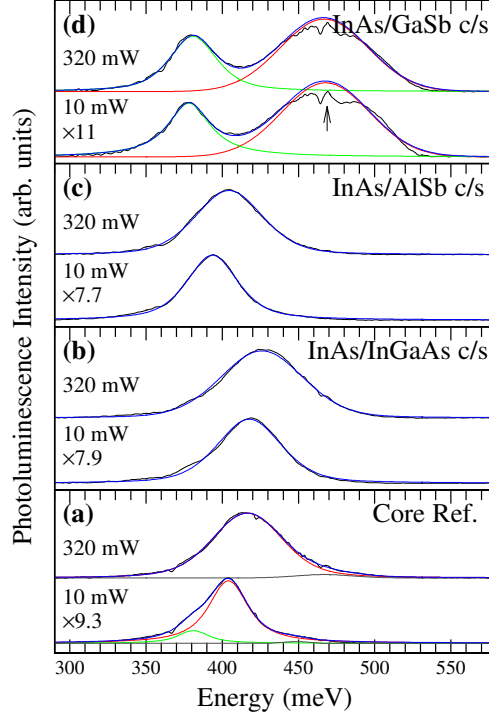
Figure 3: PL spectra and curve fittings of the (a) core reference, (b) InAs/InGaAs, (c) InAs/AlSb and (d) InAs/GaSb c/s NWs samples at 9 K under pumping powers of 10 and 320 mW, respectively. Arrow in (d) indicates atmospheric disturbance on the PL spectra.

the impurity-related transition is negligible and the type-II transition blueshifts considerably.

The InAs/InGaAs and InAs/AlSb c/s NWs samples exhibit a single Gaussian-Lorentzian PL feature, which also blueshifts obviously as the pumping power increases and is therefore ascribed to the type-II transition as well. In the InAs/InGaAs c/s NWs the type-II transition is attributed to the ZB/WZ polytypic structure, while in the InAs/AlSb c/s NWs both the polytypic structure and the type-II radial band alignment are likely responsible. The possible reason for that the PL energy of the InAs/InGaAs c/s NWs is slightly higher than that of the core reference could be the compressive strain effect of the shell on the core.[38] Also, the larger PL linewidth of the InAs/InGaAs c/s NWs accords qualitatively with more serious distortion of NW morphology.

Differing obviously from the NWs above, the InAs/GaSb c/s NWs sample exhibits two separated PL features at about 380 and 467 meV, respectively. These two features do hardly shift with pumping power and the high-energy-feature (HEF) energy is close to the band gap

of WZ InAs.[39,40] In consequence, the HEF is preliminarily assigned to the WZ InAs band-edge transition. The large PL linewidth of the HEF implies significant potential fluctuation, which agrees with the crystal disorder. The presence of the WZ InAs is a result of the GaSb-shell induced change to the InAs surface free energy.[35] Meanwhile, the low-energy-feature (LEF) is possibly associated with impurities and/or defects, due to the degradation of the crystal structure.

The assignments of type-II transitions are further affirmed by the evolution of the PL energies with pumping power, as plotted in Fig 4(a). Except for the LEF and HEF of the InAs/GaSb c/s NWs which maintain nearly unchanged, the PL features of the core reference, and the InAs/InGaAs and InAs/AlSb c/s NWs blueshift as the pumping power increases, and all the blueshifts follow quite well the equation

$$E = E_0 + kP^{1/3}, \tag{1}$$

for the band bending effect of the recombination of spatially separated carriers,[41] where E_0 is the PL energy without band bending effect, P is the pumping power, and k is a coefficient. The derived E_0 and k are 399 meV and 2.56 meV/mW$^{1/3}$ for the core reference, 414 meV and 1.76 meV/mW$^{1/3}$ for the InAs/InGaAs, and 388 meV and 2.33 meV/mW$^{1/3}$ for the InAs/AlSb c/s NWs samples, respectively. The reasonable fittings with Eq. (1) confirm the rationality of the PL features' classification.

Figure 4(b) plots the PL efficiencies against pumping power for the PL features of different NWs samples. The PL efficiency η is defined as $\eta = I/P$, the ratio of the PL integral intensity (I) to pumping power (P).[42] For comparison, the PL efficiencies at a pumping power of 10 mW are normalized to unity. Clearly, the PL efficiencies decrease monotonously as pumping power increases, which reveals the Auger recombination dominating the PL process.[43] In addition, for the InAs/GaSb c/s NWs sample, the PL efficiencies of the LEF and HEF evolve almost synchronously, which hints the defects/impurities being not photo-
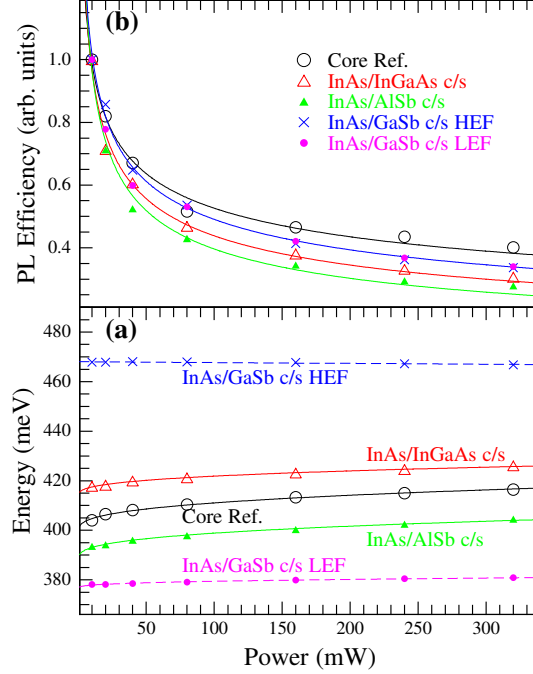
Figure 4: Evolutions of PL energy (a) and PL efficiency (b) with pumping power for different NWs samples. Solid lines in (a) represent the fits with Eq. (1), whereas dashed lines serve as guides to the eyes. PL efficiencies in (b) at a pumping power of 10 mW are normalized to unity for comparison.

excited exhaustedly during the power-dependent PL measurements. The LEF and HEF of the InAs/GaSb c/s NWs sample manifest a similar radiative recombination behavior, and can therefore be reasonably taken as an ensemble in an integral intensity analysis.

The relationship between the pumping power and the PL integral intensity can be described with the ABC model, which takes the form[44]

$$\alpha P = A(\delta n) + B(n_0 + \delta n)^2 + C(n_0 + \delta n)^2 \delta n, \qquad (2)$$

where n_0 is the density of the background carriers, δn is the density of the photo-generated carriers, α is a coefficient for the pumping efficiency, and A, B and C represent the coefficients of nonradiative, radiative and Auger recombinations, respectively. The PL integral intensity

9

can be expressed as,[44]

$$I = \beta B(n_0 + \delta n)^2 \,, \tag{3}$$

where β is a coefficient depending on the collection efficiency of the PL signal.

As Auger recombination dominates, Eq. (2) can be simplified as $\alpha P \approx C(n_0 + \delta n)^2 \delta n$. For the two extreme cases: (i) if $n_0 \gg \delta n$, then $n_0 + \delta n \approx n_0$ and $P \propto \delta n$, so the PL efficiency $\eta \propto P^{-1}$; (ii) if $\delta n \gg n_0$, then $n_0 + \delta n \approx \delta n$ and $P \propto (\delta n)^3$, and hence $\eta \propto P^{-1/3}$. Accordingly, fitting the evolution of the PL efficiency with $\eta \propto P^{\gamma}$ will disclose the relationship between n_0 and δn, and the results are depicted in Fig 4(b) as solid lines, with $\gamma = -0.27$, -0.35, -0.39 and -0.32 for the core reference, InAs/InGaAs, InAs/AlSb and InAs/GaSb c/s NWs samples, respectively. These γ values are all close to $-1/3$, and approve the validity of $\delta n \gg n_0$ for the NWs.

With such a prerequisite, the IQE of the NWs is derived,[17] and Eq. (2) is rewritten with Eq. (3) as,

$$P = aI^{1/2} + bI + cI^{3/2} \,, \tag{4}$$

where $a = A/\alpha\sqrt{\beta B}$, $b = 1/\alpha\beta$ and $c = C/\alpha\sqrt{(\beta B)^3}$. The values of a, b and c can be deduced by fitting the evolution of square root of the PL integral intensity with the pumping power. The IQE is hence described by,[17]

$$
\begin{aligned}
\mathrm{IQE} &= \frac{B(\delta n)^2}{A(\delta n) + B(\delta n)^2 + C(\delta n)^3} \\
&= \frac{bI}{aI^{1/2} + bI + cI^{3/2}} \,. \tag{5}
\end{aligned}
$$

Figure 5(a) depicts the P-$I^{1/2}$ fittings by Eq. (4) for different NWs samples. All the PL features in one spectrum are taken as an ensemble and integrated to integral intensity. The fittings are achieved with good consistency and the IQEs are derived for different NWs
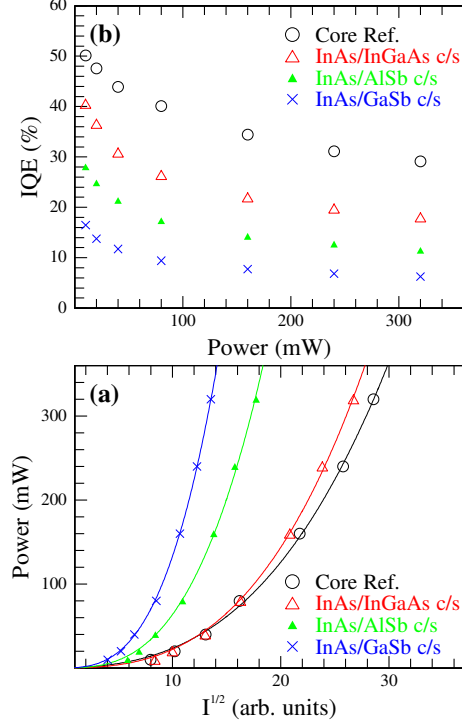
Figure 5: (a) Pumping power versus square root of PL integral intensity, and (b) derived IQE as a function of pumping power for different NWs samples.

samples at various pumping powers as plotted in Fig. 5(b).

Due to the dominant Auger recombination, the IQEs of the NWs are lower than 50% and decline monotonously as the pumping power increases. The IQE are about 50%, 41%, 28% and 16%, respectively, for the core reference, InAs/InGaAs, InAs/AlSb and InAs/GaSb c/s NWs samples with a pumping power of 10 mW, and fall down to about 29%, 18%, 11% and 6%, respectively, when the pumping power rises to 320 mW. In addition, the IQE drops in turn after the InGaAs, AlSb and GaSb shell coating. This conflicts with the prospective result that shell coating passivates the surface dislocation and enhances radiative recombination.[7,12,45] As a possible reason, the joint effects of the following issues could be considered: (i) the surface-related nonradiative channels are hardly activated at a low temperature of 9 K; (ii) the c/s lattice mismatch lowers the NW crystal quality and induces extra dislocations;[46] (iii) the stacking faults density may be enhanced due to the variation of surface free energy;[35] and (iv) the type-II radial band alignment in InAs/AlSb

11

c/s NWs reduces the overlapping of carrier wavefunction around the c/s interface[47] whereas the photo-generated carriers leak in the InAs/GaSb c/s NWs due to the type-III radial band alignment.[22]

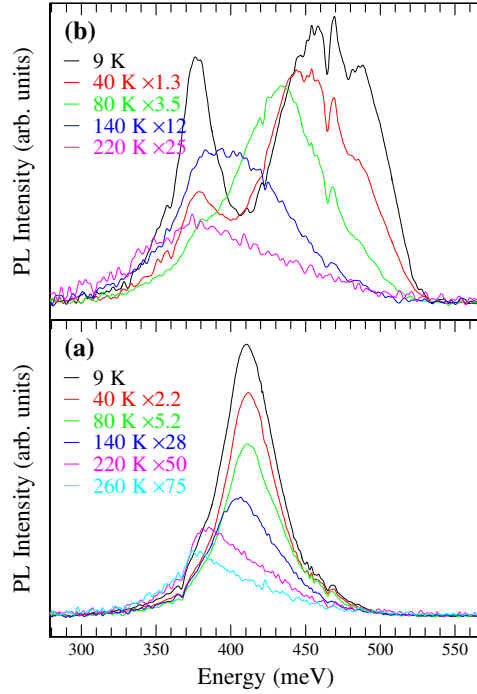
Figure 6: PL spectra of the core reference (a) and the InAs/GaSb c/s NWs (b) samples at several representative temperatures.

To active the nonradiative recombination channels, the temperature of the samples was elevated during the PL measurements. A mediate pumping power of 80 mW was selected, at which the 9-K IQEs of the core reference, InAs/InGaAs, InAs/AlSb and InAs/GaSb c/s NWs are about 40%, 26%, 17% and 9%, respectively. Fig. 6(a) and (b) depict the representative temperature-dependent PL spectra of the core reference and InAs/GaSb c/s NWs samples, respectively. The PL intensity of the core reference exhibits a dramatic attenuation as temperature rises, while the LEF of the InAs/GaSb c/s NWs diminishes and merges into HEF and the HEF dominates at temperatures above 80 K.

The IQEs at different temperatures are deduced from the temperature-dependent PL integral intensity and the 9-K IQE, with an assumption of temperature-insensitive absorption

efficiency,[48,49]

$$\text{IQE}(T) = \frac{I(T)}{I(9\,\text{K})} \times \text{IQE}(9\,\text{K})\,, \tag{6}$$

and the results are illustrated in Fig. 7(a) for the NWs samples. The IQEs decline exponentially as temperature increases, but different samples manifest different decline velocity. For example, the IQE of the InAs/InGaAs c/s NWs is lower than that of the core reference at 9 K, but is obviously higher in a temperature range of $40-140$ K. As the IQE is proportional to the PL integral intensity as describe by Eq. (6), the evolution of IQE with temperature can be fitted for identifying the possible thermal-induced nonradiative recombination channels with,[10,29,50]

$$\text{IQE}(T) \propto \frac{1}{1 + \sum \xi_j\, e^{-E_j/k_B T}}\,, \tag{7}$$

where E_j is the quenching energy of the jth nonradiative channel, ξ_j represents the nonradiative coefficient and is proportional to the ratio of nonradiative to radiative recombination probabilities, and k_B is the Boltzmann constant. While single nonradiative channel is not sufficient for fitting the IQE evolution, two channels fits the temperature range above 25 K quite well, at which dislocation-related channels dominate the nonradiative recombination. The corresponding ξ_j and E_j are derived and summarized in Table 1.

Table 1: ξ_j and E_j derived from the IQE evolution with temperature for the InAs NW core reference and the c/s NWs with InGaAs, AlSb and GaSb shells, respectively.

	Core Ref.	InGaAs shell	AlSb shell	GaSb shell
ξ_1	12.2	29.9	11.5	16.8
E_1 (meV)	8.7	18.7	12.1	12.4
ξ_2	1102	1732	346	468
E_2 (meV)	45.0	60.9	41.5	41.9

Since the IQE is derived with an approach of ensemble integral intensity, the thermal-induced IQE quenching is ascribed to the nonradiative channels related to the dislocations
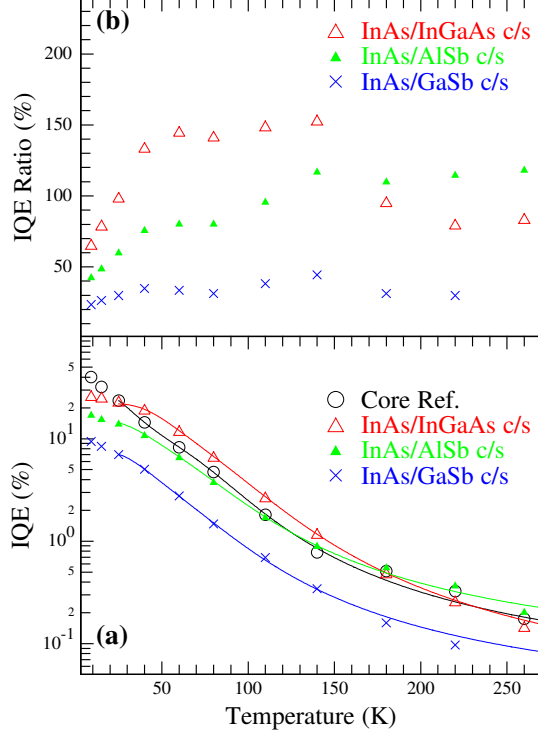
Figure 7: IQEs of different NWs samples (a) and IQE ratios of the c/s NWs to the core reference (b) as a function of temperature. Solid lines in (a) for the fittings of Eq. (7).

rather than the carriers transfer in the NWs.[10,51] In comparison with the core reference NWs, the InAs/InGaAs c/s NWs manifests quite larger activation energies E_j for the both channels, the latter may hint the thermal-quenching of the IQE to be more difficult.[52] Nevertheless, such expectation is possibly strangled by the dramatic enhancement of the nonradiative coefficient ξ_j, which is associated with the density of nonradiative impurities introduced by the degradation of crystal quality. The first nonradiative channel could be ascribed to the c/s misfit dislocations, as the dramatic increased ξ_1, about 2.5-fold to that of core reference, agrees well with the significant misfit dislocations in shell as indicated in the interface ADF image [Fig. 2(b)]. The competition between the activation energy and the nonradiative coefficient may result in a superior IQE in the c/s NWs within a narrow temperature range. This hints the importance of maintaining good crystal quality for high IQE in the type-I radial band alignment c/s NWs.

For the InAs/AlSb and InAs/GaSb c/s NWs samples the effects of shell coating on ξ_1 and

14

E_1 are relatively weak, because the c/s lattice mismatch is negligible and hence the misfit dislocation impact is inferior. The obviously smaller ξ_2 together with the almost-unchanged E_2 hints the second nonradiative channel being possibly correlated with the InAs NW surface passivation[4,7] and also indicates a reduced density of c/s interface nonradiative impurities. These suggest a more temperature-insensitive IQE, and hence a potential advantage of high-temperature IQE if the temperature-insensitive performance makes up the inherent low-temperature IQE shortage for the c/s NWs with type-II and type-III radial band alignments, even though the low-temperature IQE is lower than that of the core reference due to the spatially separation of carrier wave-function[47] and/or photo-generated carriers leakage.[22]

For further direct comparison, the IQE ratio of the c/s NWs to the core reference is depicted as a function of temperature in Fig. 7(b). At low temperatures, the surface non-radiative channels are hardly thermal-activated in the InAs NWs. The shell coating effect on the reduction of the surface dislocation is weak, and the IQE ratios are less than 100%. As temperature rises, the temperature-insensitive nature of the IQE leads to an increase to the IQE ratio. For the InAs/InGaAs c/s NWs sample, an IQE ratio of up to 150% shows up in a temperature range of $40-140$ K, despite of the morphology deterioration, indicating undoubtedly an improvement to the optical emission performance. At higher temperatures the IQE ratio falls back as the c/s strain-induced nonradiative dislocations are thermally activated and play a dominant role. For the InAs/AlSb c/s NWs sample, the IQE ratio increases monotonously, exceeds 100% at about 110 K, and goes up to 120% at a temperature of 260 K, suggesting the AlSb shell coating as a potentially effective approach for promoting high-temperature optoelectronic properties. The IQE enhancement agrees with the fact that the InAs/AlSb NW photodetector manifests the quite lower dark current than the bare InAs NW detector does.[6] For the InAs/GaSb c/s NWs sample, although the IQE ratio rises up with temperature, the type-III radial band alignment results in carrier leakage,[22] and hence the low IQE at low temperature is hardly redeemed at high temperatures. This means the GaSb shell coating may fall short of improvement to the optoelectronic performance.

Summary

To summarize, we in this work conduct pumping power- and temperature-dependent mid-infrared PL analyses on a bare InAs NWs sample as core reference and the InAs c/s NWs samples with, respectively, InGaAs, AlSb and GaSb shells. With a verified prerequisite that the contribution is negligible of background carriers to the PL intensity, the low-temperature IQEs of the NWs samples are derived from the relation of the PL integral intensity to the pumping power. The IQE drops with the shell coating, which is ascribed to the joint effect of the degradation of crystal quality due to the c/s lattice mismatch, the reduction of carrier transition efficiency due to the type-II radial band alignment, and the leakage of photo-generated carriers in the type-III band alignment.

In comparison with the bare core reference, the c/s NWs with InGaAs shell coating exhibits a larger quenching activation energy and nonradiative coefficient, which results in a considerable IQE improvement in a temperature range of $40-140$ K. For the c/s NWs with AlSb and GaSb shells, the shell coating reduces the surficial nonradiative dislocations, and leads the IQE to be temperature-insensitive. The c/s NWs with AlSb shell coating manifests an improved IQE at temperatures above 110 K, but that with GaSb shell coating doesn't because of the broken-gap type-III radial band alignment and the resultant carriers leakage. These results deepen the understanding of the shell coating effects on InAs NWs, suggest appropriate shells for optimizing optoelectronic performance, reveal the potentiality of the type-I and -II c/s NWs for acquiring temperature-insensitive IQE, and demonstrate the pumping power- and temperature-dependent mid-infrared PL spectroscopy as an efficacious approach for IQE analysis in narrow-gap NWs.

Acknowledgement

References

(1) Sumikura, H.; Zhang, G.; Takiguchi, M.; Takemura, N.; Shinya, A.; Gotoh, H.; Notomi, M. Mid-Infrared Lasing of Single Wurtzite InAs Nanowire. Nano Lett. **2019**, 19, 8059–8065.

(2) Wei, W.; Bao, X.-Y.; Soci, C.; Ding, Y.; Wang, Z.-L.; Wang, D. Direct heteroepitaxy of vertical InAs nanowires on Si substrates for broad band photovoltaics and photodetection. Nano Lett. **2009**, 9, 2926–2934.

(3) Ren, D.; Meng, X.; Rong, Z.; Cao, M.; Farrell, A. C.; Somasundaram, S.; Azizurrahman, K. M.; Williams, B. S.; Huffaker, D. L. Uncooled Photodetector at Short-Wavelength Infrared Using InAs Nanowire Photoabsorbers on InP with p–n Heterojunctions. Nano Lett. **2018**, 18, 7901–7908.

(4) Treu, J.; Bormann, M.; Schmeiduch, H.; Doeblinger, M.; Morkoetter, S.; Matich, S.; Wiecha, P.; Saller, K.; Mayer, B.; Bichler, M.; Amann, M.-C.; Finley, J. J.; Abstreiter, G.; Koblmueller, G. Enhanced Luminescence Properties of InAs–InAsP Core–Shell Nanowires. Nano Lett. **2013**, 13, 6070–6077.

(5) Li, X.; Zhang, K.; Treu, J.; Stampfer, L.; Koblmueller, G.; Toor, F.; Prineas, J. P. Contactless Optical Characterization of Carrier Dynamics in Free-Standing InAs-InAlAs Core–Shell Nanowires on Silicon. Nano Lett. **2019**, 19, 990–996.

(6) Li, H.; Alradhi, H.; Jin, Z.; Anyebe, E.; Sanchez, A. M.; Linhart, W. M.; Kudrawiec, R.; Fang, H.; Wang, Z.; Hu, W.; Zhuang, Q. Novel Type-II InAs-AlSb Core-Shell Nanowires and Their Enhanced Negative Photocurrent for Efficient Photodetection. Adv. Funct. Mater. **2018**, 28, 1705382.

(7) Jurczak, P.; Zhang, Y.; Wu, J.; Sanchez, A. M.; Aagesen, M.; Liu, H. Ten-Fold Enhancement of InAs Nanowire Photoluminescence Emission with an InP Passivation Layer. Nano Lett. **2017**, 17, 3629–3633.

(8) Speckbacher, M.; Treu, J.; Whittles, T. J.; Linhart, W. M.; Xu, X.; Saller, K.; Dhanak, V. R.; Abstreiter, G.; Finley, J. J.; Veal, T. D.; Koblmüller, G. Direct Measurements of Fermi Level Pinning at the Surface of Intrinsically n-Type InGaAs Nanowires. Nano Lett. **2016**, 16, 5135–5142.

(9) Alhodaib, A.; Noori, Y.; Carrington, P. J.; Sanchez, A. M.; Thompson, M. D.; Young, R. J.; Krier, A.; Marshall, A. R. J. Room temperature mid-infrared emission from faceted InAsSb multi quantum wells embedded in InAs nanowires. Nano Lett. **2018**, 18, 235–240.

(10) Chen, X.; Zhuang, Q.; Alradhi, H.; Jin, Z. M.; Zhu, L.; Chen, X.; Shao, J. Midinfrared Photoluminescence up to 290 K Reveals Radiative Mechanisms and Substrate Doping-Type Effects of InAs Nanowires. Nano Lett. **2017**, 17, 1545.

(11) Bao, J.; Bell, D. C.; Capasso, F.; Wagner, J. B.; Martensson, T.; Tragardh, J.; Samuelson, L. Optical properties of rotationally twinned InP nanowire heterostructures. Nano Lett. **2008**, 8, 836–841.

(12) Ji, X.; Chen, X.; Yang, X.; Zhang, X.; Shao, J.; Yang, T. Self-Seeded MOCVD Growth and Dramatically Enhanced Photoluminescence of InGaAs/InP Core–Shell Nanowires. Nanoscale Res. Lett. **2018**, 13, 269.

(13) Svensson, J.; Anttu, N.; Vainorius, N.; Borg, B. M.; Wernersson, L. Diameter-Dependent Photocurrent in InAsSb Nanowire Infrared Photodetectors. Nano Lett. **2013**, 13, 1380–1385.

(14) Cao, L.; White, J. S.; Park, J.; Schuller, J. A.; Clemens, B. M.; Brongersma, M. L.

Engineering light absorption in semiconductor nanowire devices. Nature Mater. **2009**, 8, 643–647.

(15) Kempa, T. J.; Cahoon, J. F.; Kim, S. K.; Day, R. W.; Bell, D. C.; Park, H.; Lieber, C. M. Coaxial multishell nanowires with high-quality electronic interfaces and tunable optical cavities for ultrathin photovoltaics. Proc. Natl. Acad. Sci. USA **2012**, 109, 1407–1412.

(16) Fadaly, E. M. T. et al. Direct-bandgap emission from hexagonal Ge and SiGe alloys. Nature **2020**, 580, 205–209.

(17) Yoo, Y.; Roh, T.; Na, J.; Son, S. J.; Cho, Y. Simple analysis method for determining internal quantum efficiency and relative recombination ratios in light emitting diodes. Appl. Phys. Lett. **2013**, 102, 211107.

(18) Jiang, X.; Xiong, Q.; Nam, S.; Qian, F.; Li, Y.; Lieber, C. M. InAs/InP Radial Nanowire Heterostructures as High Electron Mobility Devices. Nano Lett. **2007**, 7, 3214–3218.

(19) Popovitzbiro, R.; Kretinin, A. V.; Von Huth, P.; Shtrikman, H. InAs/GaAs Core–Shell Nanowires. Cryst. Growth Des. **2011**, 11, 3858–3865.

(20) Rocci, M.; Rossella, F.; Gomes, U. P.; Zannier, V.; Rossi, F.; Ercolani, D.; Sorba, L.; Beltram, F.; Roddaro, S. Tunable Esaki Effect in Catalyst-Free InAs/GaSb Core–Shell Nanowires. Nano Lett. **2016**, 16, 7950–7955.

(21) Pistol, M.; Pryor, C. E. Band structure of core-shell semiconductor nanowires. Phys. Rev. B **2008**, 78, 115319.

(22) Kishore, V. V. R.; Partoens, B.; Peeters, F. M. Electronic structure of InAs/GaSb core-shell nanowires. Phys. Rev. B **2012**, 86, 165439.

(23) Kavanagh, K. L.; Salfi, J.; Savelyev, I.; Blumin, M.; Ruda, H. E. Transport and strain relaxation in wurtzite InAs–GaAs core-shell heterowires. Appl. Phys. Lett. **2011**, 98, 152103.

(24) Shao, J.; Lu, W.; Lü, X.; Yue, F.; Li, Z.; Guo, S.; Chu, J. Modulated photoluminescence spectroscopy with a step-scan Fourier transform infrared spectrometer. Rev. Sci. Instrum. **2006**, 77, 063104.

(25) Zha, F. X.; Shao, J.; Jiang, J.; Yang, W. Y. "Blueshift" in photoluminescence and photovoltaic spectroscopy of the ion-milling formed n-on-p HgCdTe photodiodes. Appl. Phys. Lett. **2007**, 90, 201112.

(26) J. Shao,; L. Chen,; X. Lü,; W. Lu,; L. He,; S. Guo,; J. Chu, Realization of photoreflectance spectroscopy in very-long wave infrared of up to 20 μm. Appl. Phys. Lett. **2009**, 95, 041908.

(27) Shao, J.; Chen, L.; Lu, W.; Lü, X.; Zhu, L.; Guo, S.; He, L.; Chu, J. Backside-illuminated infrared photoluminescence and photoreflectance: Probe of vertical nonuniformity of HgCdTe on GaAs. Appl. Phys. Lett. **2010**, 96, 121915.

(28) Zhang, X.; Shao, J.; Chen, L.; Lü, X.; Guo, S.; He, L.; Chu, J. Infrared photoluminescence of arsenic-doped HgCdTe in a wide temperature range of up to 290 K. J. Appl. Phys. **2011**, 110, 043503.

(29) Shao, J.; Lu, W.; Tsen, G.; Guo, S.; Dell, J. Mechanisms of infrared photoluminescence in HgTe/HgCdTe superlattice. J. Appl. Phys. **2012**, 112, 063512.

(30) Chen, X.; Zhou, Y.; Zhu, L.; Qi, Z.; Xu, Q.; Xu, Z.; Guo, S.; Chen, J.; He, L.; Shao, J. Evolution of interfacial properties with annealing in InAs/GaSb superlattice probed by infrared photoluminescence. Jpn. J. Appl. Phys. **2014**, 53, 082201.

(31) Chen, X.; Xing, J.; Zhu, L.; Zha, F. X.; Niu, Z.; Guo, S.; Shao, J. GaInSb/InAs/AlSb quantum wells with InSb- and GaAs-like interfaces investigated by temperature- and magnetic field-dependent photoluminescence. J. Appl. Phys. **2016**, 119, 175301.

(32) Gagliano, L.; Albani, M.; Verheijen, M. A.; Bakkers, E. P. A. M.; Miglio, L. Twofold origin of strain-induced bending in core-shell nanowires: The GaP/InGaP case. Nanotechnology **2018**, _29_, 315703.

(33) Lewis, R. B.; Corfdir, P.; Kupers, H.; Flissikowski, T.; Brandt, O.; Geelhaar, L. Nanowires Bending over Backward from Strain Partitioning in Asymmetric Core–Shell Heterostructures. Nano Lett. **2018**, _18_, 2343–2350.

(34) Luo, N.; Huang, G. Y.; Liao, G.; Ye, L. H.; Xu, H. Band-inverted gaps in InAs/GaSb and GaSb/InAs core-shell nanowires. Sci. Rep. **2016**, _6_, 38698.

(35) Anyebe, E. A.; Sanchez, A. M.; Hindmarsh, S.; Chen, X.; Shao, J.; Rajpalke, M. K.; Veal, T. D.; Robinson, B. J.; Kolosoy, O.; Anderson, F.; Sundaram, R.; Wang, Z. M.; Falko, V.; Zhuang, Q. Realization of Vertically Aligned, Ultrahigh Aspect Ratio InAsSb Nanowires on Graphite. Nano Lett. **2015**, _15_, 4348–4355.

(36) Chen, X.; Xu, Z.; Zhou, Y.; Zhu, L.; Chen, J.; Shao, J. Evaluating interface roughness and micro-fluctuation potential of InAs/GaSb superlattices by mid-infrared magnetophotoluminescence. Appl. Phys. Lett. **2020**, _117_, 081104.

(37) Chen, X.; Wu, X.; Yue, L.; Zhu, L.; Pan, W.; Qi, Z.; Wang, S.; Shao, J. Negative thermal quenching of below-bandgap photoluminescence in InPBi. Appl. Phys. Lett. **2017**, _110_, 051903.

(38) Rajadell, F.; Royo, M.; Planelles, J. Strain in free standing CdSe/CdS core-shell nanorods. J. Appl. Phys. **2012**, _111_, 014303.

(39) Rota, M. B.; Ameruddin, A. S.; Fonseka, H. A.; Gao, Q.; Mura, F.; Polimeni, A.; Miriametro, A.; Tan, H. H.; Jagadish, C.; Capizzi, M. Bandgap Energy of Wurtzite InAs Nanowires. Nano Lett. **2016**, _16_, 5197–5203.

(40) De, A.; Pryor, C. E. Predicted band structures of III-V semiconductors in the wurtzite phase. Phys. Rev. B **2010**, _81_, 155210.

(41) Alonsoalvarez, D.; Alen, B.; Garcia, J. M.; Ripalda, J. M. Optical investigation of type II GaSb/GaAs self-assembled quantum dots. Appl. Phys. Lett. **2007**, _91_, 263103.

(42) Quitsch, W.; Sager, D.; Loewenich, M.; Meyer, T.; Hahn, B.; Bacher, G. Low injection losses in InGaN/GaN LEDs: The correlation of photoluminescence, electroluminescence, and photocurrent measurements. J. Appl. Phys. **2018**, _123_, 214502.

(43) Cho, Y.; Lue, X.; Wienold, M.; Ramsteiner, M.; Grahn, H. T.; Brandt, O. Auger recombination as the dominant nonradiative recombination channel in InN. Phys. Rev. B **2013**, _87_, 155203.

(44) Seetoh, I.; Soh, C.; Fitzgerald, E.; Chua, S. Auger recombination as the dominant recombination process in indium nitride at low temperatures during steady-state photoluminescence. Appl. Phys. Lett. **2013**, _102_, 101112.

(45) Dan, Y.; Seo, K.; Takei, K.; Meza, J. H.; Javey, A.; Crozier, K. B. Dramatic Reduction of Surface Recombination by in Situ Surface Passivation of Silicon Nanowires. Nano Lett. **2011**, _11_, 2527–2532.

(46) Kavanagh, K. L. Misfit dislocations in nanowire heterostructures. Semicond. Sci. Technol. **2010**, _25_, 024006.

(47) Kroemer, H. The 6.1 A family (InAs, GaSb, AlSb) and its heterostructures: a selective review. Physica E **2004**, _20_, 196.

(48) Brault, J.; Matta, S.; Ngo, T.; Khalfioui, M. A.; Valvin, P.; Leroux, M.; Damilano, B.; Korytov, M.; Brandli, V.; Vennegues, P.; Massies, J.; Gil, B. Internal quantum efficiencies of AlGaN quantum dots grown by molecular beam epitaxy and emitting in the UVA to UVC ranges. J. Appl. Phys. **2019**, _126_, 205701.

(49) Watanabe, S.; Yamada, N.; Nagashima, M.; Ueki, Y.; Sasaki, C.; Yamada, Y.; Taguchi, T.; Tadatomo, K.; Okagawa, H.; Kudo, H. Internal quantum efficiency of highly-efficient $In_xGa_{1-x}N$-based near-ultraviolet light-emitting diodes. Appl. Phys. Lett. **2003**, <u>83</u>, 4906–4908.

(50) Sun, H.; Calvez, S.; Dawson, M.; Gupta, J.; Aers, G.; Sproule, G. Thermal quenching mechanism of photoluminescence in 1.55 μm GaInNAsSb/Ga(N)As quantum-well structures. Appl. Phys. Lett. **2006**, <u>89</u>, 101909.

(51) Reshchikov, M. A. Temperature dependence of defect-related photoluminescence in III-V and II-VI semiconductors. J. Appl. Phys. **2014**, <u>115</u>, 012010.

(52) Sun, Y.; Cho, Y.; Kim, H.; Kang, T. W. High efficiency and brightness of blue light emission from dislocation-free InGaN/GaN quantum well nanorod arrays. Appl. Phys. Lett. **2005**, <u>87</u>, 093115.

Graphical TOC Entry
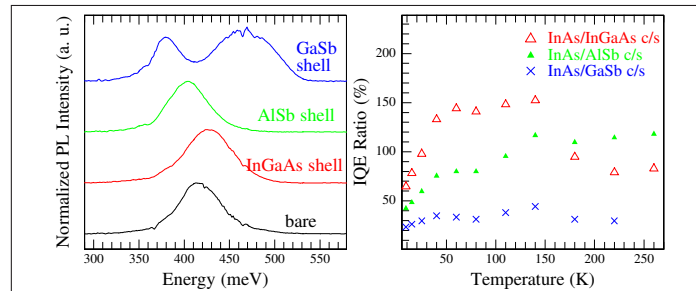
(Left) 9-K PL spectra of bare InAs NWs and InAs core/shell NWs with different shells; (Right) IQE ratio of core/shell NWs to bare NWs as a function of temperature.